

## Article

# Effects of MgO and Rare-Earth Oxides ( $Y_2O_3$ , $Yb_2O_3$ , $Dy_2O_3$ ) on the Structural Characteristics and Electrical Properties of $BaTiO_3$

Jae Hoon Park and Eung Soo Kim \* 

Department of Advanced Materials Engineering, Graduate School, Kyonggi University, Suwon 16227, Republic of Korea

\* Correspondence: eskim@kyonggi.ac.kr; Tel.: +82-31-249-9764

**Abstract:** This study investigated the impact of MgO and rare-earth oxides ( $Y_2O_3$ ,  $Yb_2O_3$ , and  $Dy_2O_3$ ) on the structural characteristics and electrical properties of  $BaTiO_3$ . Specimens sintered at 1350 °C for durations ranging from 1 to 5 h in air exhibited a single phase of  $BaTiO_3$  with a tetragonal structure. This was observed for pure  $BaTiO_3$  and specimens co-doped with MgO- $Y_2O_3$  and/or MgO- $Dy_2O_3$ . However, a pseudo-cubic structure of  $BaTiO_3$  was detected for specimens doped with MgO or co-doped with MgO- $Yb_2O_3$ . The unit-cell volume of the sintered specimens was found to be dependent on the type of substitution ion for the A/B site of  $BaTiO_3$  ( $ABO_3$ ). The dielectric constant ( $\epsilon_r$ ) of the sintered specimens decreased with the substitution of MgO and rare-earth oxides due to a decrease in tetragonality ( $c/a$ ). The electrical resistivities of the sintered specimens were influenced not only by their microstructural characteristics but also by the secondary phases of the sintered specimens. The  $BaTiO_3$  specimens co-doped with MgO- $Yb_2O_3$  and/or doped with MgO met the EIA X7R and X8R specifications ( $-55$  to  $125\sim 150$  °C,  $\Delta C/C = \pm 15\%$  or less), respectively.

**Keywords:**  $BaTiO_3$ ; MgO; rare-earth oxides; Rietveld refinement; electrical properties



**Citation:** Park, J.H.; Kim, E.S. Effects of MgO and Rare-Earth Oxides ( $Y_2O_3$ ,  $Yb_2O_3$ ,  $Dy_2O_3$ ) on the Structural Characteristics and Electrical Properties of  $BaTiO_3$ . *Processes* **2023**, *11*, 3235. <https://doi.org/10.3390/pr11113235>

Academic Editors: Andrey Yurkov, Denis Kuznetsov and Maria Vartanyan

Received: 28 October 2023  
Revised: 11 November 2023  
Accepted: 14 November 2023  
Published: 16 November 2023



**Copyright:** © 2023 by the authors. Licensee MDPI, Basel, Switzerland. This article is an open access article distributed under the terms and conditions of the Creative Commons Attribution (CC BY) license (<https://creativecommons.org/licenses/by/4.0/>).

## 1. Introduction

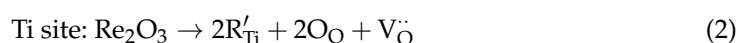
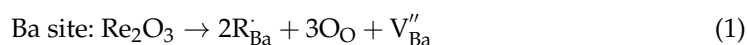
The ongoing advancement of electronic devices has led to an escalating demand for the miniaturisation and enhancement of electronic components. Multilayer ceramic capacitors (MLCCs), due to their high volumetric efficiency and stability, have become a crucial passive component. The increasing application of MLCCs has necessitated a fundamental investigation into their high dielectric constant ( $\epsilon_r$ ) and thermal stability. Specifically, the industry has formulated the X7R and X8R standards ( $\Delta C/C \sim \pm 15\%$  and  $-50\sim 125$  °C,  $150$  °C, respectively), as thermal stability limits the application of MLCCs [1–4].

To achieve a high dielectric constant, it is necessary to thin the dielectric layer of MLCCs by decreasing the particle size of  $BaTiO_3$  (barium titanate, BT), which is one of the primary raw materials due to its high dielectric constant ( $\epsilon_r$ ) [5]. Therefore, many studies have been conducted to identify methods that can control the morphology of BT particles, such as the sol-gel method, hydrothermal method, and solvothermal method [6–9]. For example, the sol-gel method provides a high purity of products and a relatively low synthesis temperature [7,8]. However, the calcination step at 700 °C or over induces coarse and chemically bonded aggregates. Zhou et al. [6] reported preparing BT nanoparticles using a hydrothermal method from two different starting materials. BT nanoparticles prepared from titanium hydroxide and barium hydroxide showed a spherical grain size of 65 nm with a narrow size distribution, while those prepared from barium hydroxide and titanium dioxide showed coarse particles arising from lattice defects, which were compensated by the presence of cation vacancies [6]. A solvothermal method for synthesizing BT nanoparticles in large batches at room temperature was reported by Wei et al. [9]. By adjusting the ratio of the solvent mixture and the reaction time, the particle size of the BT can be modulated within the range of 7 nm to 16 nm, showing a narrow size distribution. Based

on these considerations, the starting materials and the solvent are important factors when synthesizing BT nanoparticles.

Furthermore, a narrow nanoparticle size distribution of dopant oxides such as NiO, MgO, and SiO<sub>2</sub> is important for the performance of MLCCs. Most common methods for obtaining nanosized doping particles for BT, such as MgO, SiO<sub>2</sub> and Al<sub>2</sub>O<sub>3</sub>, are modified from the Pechini method, which is based on the abilities of organic compounds. Organic compounds such as acids, carbohydrates, and alcohols are used as chelating agents for the metal ions. Due to the formation of a polymer network with a homogeneous structure and a uniform distribution of ions during polyesterification, a final product with a good dispersion can be obtained. The formation of oxide nanoparticles occurs in the reaction space, which is concentrated in the walls of the cellular structure during swelling of the polymer network in the intermediate form stage and is determined by the processing temperature. In addition, the average particle size of nano oxides can be determined by the wall thickness in the polymer network. Kozerozhets et al. obtained MgO, SiO<sub>2</sub>, and Al<sub>2</sub>O<sub>3</sub> nanoparticle oxides within an average particle size of 20 nm to 30 nm by modifying the Pechini method [10].

Another way to improve the dielectric constant of MLCCs is to substitute proper ions in the BT lattice. There have been many studies to investigate the effect of various additives on the dielectric properties of BT [11–17], since the dielectric properties of BT could be changed according to the valence state of the dopant and its substitution site in a BT lattice. Especially, many rare-earth oxides are used as dopants due to their amphoteric characteristics to improve the dielectric properties of BT, and previous studies have reported that the ionic radius of rare-earth oxides is a crucial factor when they are substituted into a BT lattice. Smaller ions occupy the Ti site, and larger ones occupy the Ba site. Intermediate ions such as Dy, Y, and Ho could occupy both the Ba and Ti sites depending on the Ba/Ti ratio of BT and the sintering temperature [13–17]. Rare-earth oxides with an intermediate ionic size are known to act as a donor when incorporated into the Ba site and as an acceptor in the Ti site as follows:



Donors and acceptors are useful in capturing oxygen vacancies bound to free electrons, reducing carrier concentrations, and thereby improving the anti-reduction performance of BT ceramics [18].

Thermal stability is another important factor for the applications of MLCCs. However, the nonlinear dielectric behaviour of pure BT with temperature, caused by phase transitions (rhombohedral to orthorhombic at  $-90^\circ\text{C}$ , orthorhombic to tetragonal at  $0^\circ\text{C}$ , tetragonal to cubic at  $125^\circ\text{C}$ ), results in an unstable temperature dependence of the dielectric constant. Therefore, the composition of BT is controlled by doping elements such as Mg<sup>2+</sup>, Ca<sup>2+</sup>, and Zr<sup>4+</sup> ions to suppress or shift the Curie temperature [4,5,11,12]. Rare-earth oxides also have an influence on the thermal stability of BT, forming core-shell structures in the BT grains. In this structure, the shell comprises a non-ferroelectric pseudo-cubic structure created by the partial substitution of dopants, while the core contains ferroelectric BT with a tetragonal structure. Consequently, the dielectric characteristics and thermal stability of BT can be regulated by varying the amount and type of rare-earth oxides.

Numerous studies have been conducted on BaTiO<sub>3</sub> doped with MgO and rare-earth oxides. Kishi et al. reported the formation mechanism of a core-shell structure in the BaTiO<sub>3</sub>-MgO-Ho<sub>2</sub>O<sub>3</sub> system. At a low temperature, the shell phase is formed by a reaction between MgO and BT, and then Ho<sub>2</sub>O<sub>3</sub> reacts with the shell at a high temperature. The diffusion of Ho<sub>2</sub>O<sub>3</sub> is hindered by MgO, inhibiting grain growth [19]. Pu et al. explored the effect of a grain growth inhibitor of Dy ions for the formula Ba<sub>1-x</sub>Dy<sub>2x/3</sub>TiO<sub>3</sub> and obtained an increased dielectric constant ( $\epsilon_r$ ) for  $x = 0.75$  [1]. Kim et al. investigated the role of

MgO and Y<sub>2</sub>O<sub>3</sub> in the BT-MgCO<sub>3</sub>-Y<sub>2</sub>O<sub>3</sub>-BaCO<sub>3</sub>-SiO<sub>2</sub> system. They found that Y<sub>2</sub>O<sub>3</sub> plays a dominant role in the formation of the shell by easily dissolving into BT, while MgO tends to stay at the grain boundary [13]. Additionally, Y<sub>2</sub>O<sub>3</sub> flattened the dielectric constant temperature (the  $\epsilon_r$ -T curve) for BT-Y<sub>2</sub>O<sub>3</sub>-MgO without shifting the Curie peak of BT [20]. Wang et al. reported the effect of the sintering atmosphere on the microstructure and dielectric properties of specimens co-doped with Yb/Mg [21].

However, most studies have focused on the effect of MgO and rare-earth oxides on the microstructural characteristics and the temperature stability of the dielectric constant. In light of these considerations, this study investigated the effects of MgO and rare-earth oxides (Y<sub>2</sub>O<sub>3</sub>, Yb<sub>2</sub>O<sub>3</sub>, and Dy<sub>2</sub>O<sub>3</sub>) on the structural characteristics and electrical properties of BT. The aim was to propose relationships between the structural characteristics and electrical properties of BT.

## 2. Materials and Methods

BaTiO<sub>3</sub> (170 nm, Fuji Titanium Ind. Co., Osaka, Japan), MgO (Fine Material, Seongnam, Republic of Korea), Dy<sub>2</sub>O<sub>3</sub> (Solvay, Brussels, Belgium), Y<sub>2</sub>O<sub>3</sub> (Solvay, Brussels, Belgium), and Yb<sub>2</sub>O<sub>3</sub> (Solvay, Brussels, Belgium) were utilised as starting materials. These were mixed in stoichiometric ratios as per Table 1. The mixed powders were milled with yttrium-stabilised zirconia balls for 24 h in ethyl alcohol and then dried. The dried powders were isostatically pressed into pellets under a pressure of 500 kg/cm<sup>2</sup> using 15 mm diameter disks. The pressed disks were sintered at 1350 °C for durations ranging from 1 to 5 h in an air atmosphere.

**Table 1.** Composition of the BaTiO<sub>3</sub> specimens doped with MgO and/or co-doped with MgO-Re<sub>2</sub>O<sub>3</sub> (Re = Y, Yb, or Dy) [unit: mol].

Additives	Abbreviation	BaTiO <sub>3</sub>	MgO	Y <sub>2</sub> O <sub>3</sub>	Yb <sub>2</sub> O <sub>3</sub>	Dy <sub>2</sub> O <sub>3</sub>
Pure BaTiO <sub>3</sub>	BT	100	0	0	0	0
MgO	Mg	100	1	0	0	0
MgO-Y <sub>2</sub> O <sub>3</sub>	Mg/Y	100	1	1	0	0
MgO-Yb <sub>2</sub> O <sub>3</sub>	Mg/Yb	100	1	0	1	0
MgO-Dy <sub>2</sub> O <sub>3</sub>	Mg/Dy	100	1	0	0	1

The crystalline phases of the sintered specimens were analysed using X-ray diffraction (XRD, D/max-2500V/PC, Rigaku, Tokyo) over the range of  $2\theta = 10\text{--}80^\circ$ . Rietveld refinement (RIR) measurements were performed on the XRD data using Fullprof software (version 7.95) to obtain structural characteristics such as the lattice parameters, tetragonality ( $c/a$ ), and unit-cell volume of the sintered specimens. Silver electrodes were coated on both surfaces of the sintered specimens and fired at 550 °C for 30 min. The microstructures of the sintered specimens were observed using a scanning electron microscope (SEM, Su-70, Hitachi, Japan). Apparent densities and relative densities of the sintered specimens were obtained by the Archimedes method and Rietveld refinement, respectively. The dielectric constants of the specimens were determined from their measured capacitances (pF) using a Capacitance Meter (E4981A, KEYSIGHT, Santa Rosa, CA, USA) at 1 KHz. The resistivities ( $\rho$ ) of the specimens were calculated using a High Resistance Meter (4339B, KEYSIGHT, Santa Rosa, CA, USA) at 500 V for 60 s. The temperature coefficient of capacitance of the specimens was measured using a temperature coefficient of capacitance (TCC) measurement system (TM-100, NANOIONICS KOREA, Gangneung-si, Gangwon-do, Republic of Korea) from  $-50\text{ }^\circ\text{C}$  to  $150\text{ }^\circ\text{C}$  at 1 KHz.

## 3. Results and Discussion

### 3.1. Physical Properties

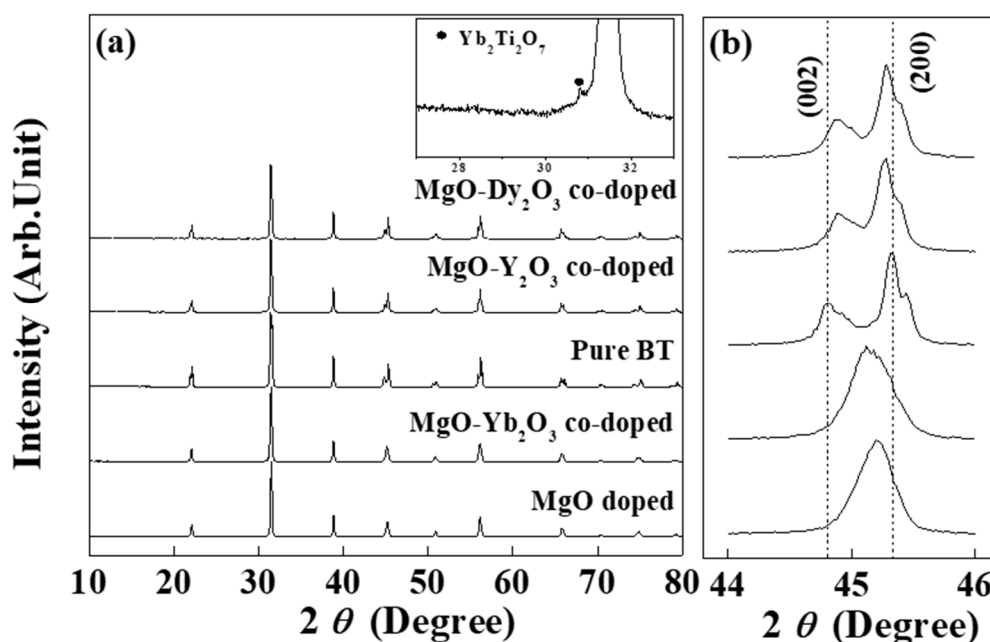
According to the report of Gong et al. [22], the relative density is a critical factor for dielectric materials. It could affect not only the formation of a core shell for BT substituted with rare-earth oxides but also the thermal stability of the BT. Therefore, the sintering

condition of BT specimens doped with MgO and/or co-doped with MgO-Re<sub>2</sub>O<sub>3</sub> (with Re representing Y, Yb, or Dy) was optimised to achieve a higher relative density above 94% of the theoretical value, as listed in Table 2. This was performed to neglect the effect of pores on the dielectric and electrical properties of the sintered specimens, which will be discussed in Section 3.2.

**Table 2.** Relative densities of the BaTiO<sub>3</sub> specimens doped with MgO and/or co-doped with MgO-Re<sub>2</sub>O<sub>3</sub> (Re = Y, Yb, or Dy) sintered at 1350 °C for 1–5 h in air.

Specimen	Sintering Condition (°C/h)	Apparent Density (g/cm <sup>3</sup> )	Theoretical Density (g/cm <sup>3</sup> )	Relative Density (%)
MgO-Dy <sub>2</sub> O <sub>3</sub>	1350 °C/1 h	5.8140	6.0200	96.58
Pure BT		5.8030	6.0018	96.42
MgO-Y <sub>2</sub> O <sub>3</sub>		5.7845	6.0170	96.14
MgO	1350 °C/5 h	5.6686	6.0080	94.35
MgO-Yb <sub>2</sub> O <sub>3</sub>		5.7683	6.0170	95.87

The XRD patterns of the BT specimens doped with MgO and/or co-doped with MgO-Re<sub>2</sub>O<sub>3</sub> (with Re representing Y, Yb, or Dy) sintered at 1350 °C for 1–5 h in air are presented in Figure 1a. All of the sintered specimens, except for those co-doped with MgO-Yb<sub>2</sub>O<sub>3</sub>, exhibited a single phase of BaTiO<sub>3</sub> with a perovskite structure. However, the secondary phase of pyrochlore Yb<sub>2</sub>Ti<sub>2</sub>O<sub>7</sub> (ICCD No. 98-017-3750) was detected for the specimens co-doped with MgO-Yb<sub>2</sub>O<sub>3</sub>, while a single phase of BT was obtained for the MgO-doped and MgO-Y<sub>2</sub>O<sub>3</sub>/MgO-Dy<sub>2</sub>O<sub>3</sub> co-doped specimens. The formation of the Yb<sub>2</sub>Ti<sub>2</sub>O<sub>7</sub> secondary phase is due to the smaller solubility of Yb<sub>2</sub>O<sub>3</sub> than that of Y<sub>2</sub>O<sub>3</sub> and Dy<sub>2</sub>O<sub>3</sub>. Rare-earth oxides are forced to substitute at the Ba site of BT for the BT-MgO-Re<sub>2</sub>O<sub>3</sub> (with Re representing Y, Yb, or Dy) system due to the substitution of the Mg<sup>2+</sup> ion for the Ti<sup>4+</sup> ion. However, Yb<sub>2</sub>O<sub>3</sub> acts as an acceptor due to its smaller ionic radius than Y<sup>3+</sup> and Dy<sup>3+</sup> ions [23]. Thus, extra Yb<sub>2</sub>O<sub>3</sub> may react with TiO<sub>2</sub>, forming a Yb<sub>2</sub>Ti<sub>2</sub>O<sub>7</sub> phase.



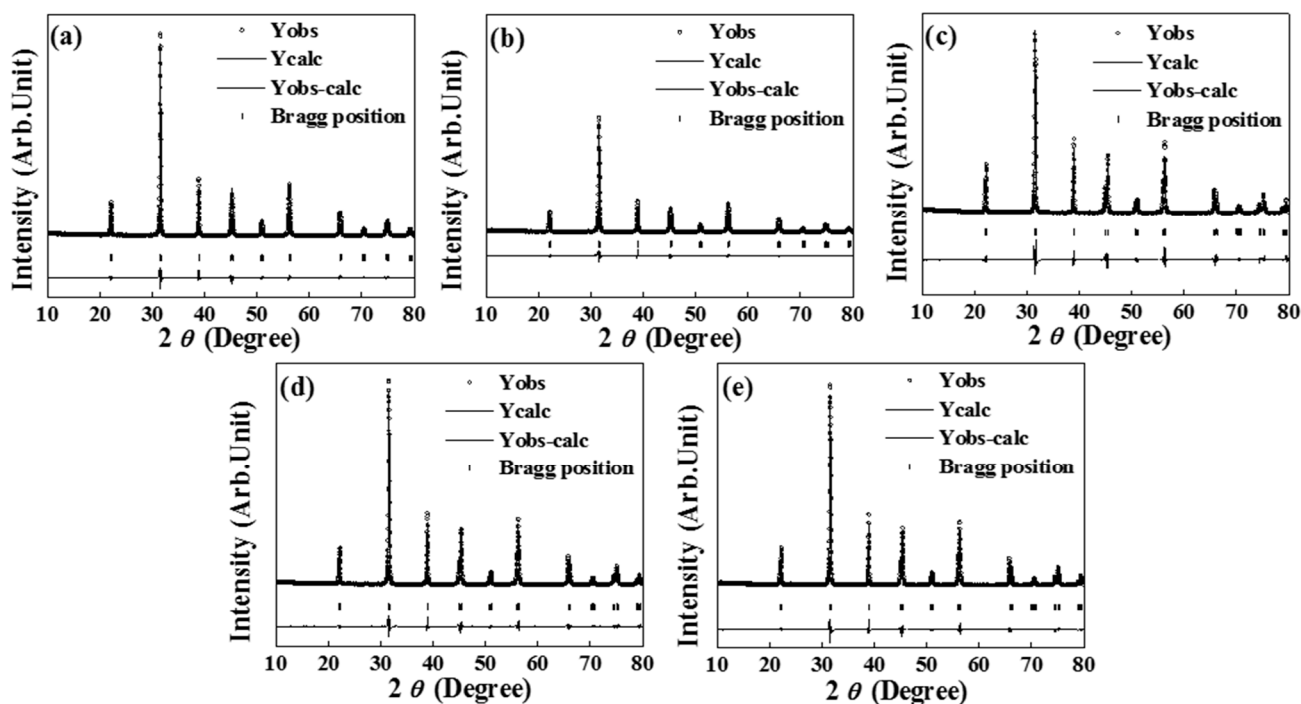
**Figure 1.** (a) XRD patterns of the sintered specimens doped with MgO and co-doped with MgO-Re<sub>2</sub>O<sub>3</sub> (Re = Y, Yb, or Dy) and (b) the enlarged XRD patterns of the sintered specimens in the range of 2θ from 44° to 46°.

Figure 1b displays the enlarged XRD patterns of the sintered specimens over the range of  $2\theta = 42\text{--}48^\circ$ . The crystal structure of  $\text{BaTiO}_3$  ceramics can be determined by the splitting of (002) and (200) peaks over the range of  $2\theta = 44\text{--}46^\circ$  [24]. The sintered pure BT and the sintered specimens co-doped with  $\text{MgO}\text{-Y}_2\text{O}_3$  and  $\text{MgO}\text{-Dy}_2\text{O}_3$  exhibited a tetragonal structure (ICCD No. 01-081-2202) of BT with peak splitting of the (002) and (200) planes. Rare-earth oxides play a dominant role in the formation of a core-shell structure in the  $\text{BaTiO}_3$  grain, and they exist at a shell of  $\text{BaTiO}_3$  grain, as described above [13]. The migration of rare-earth oxides into the core grain of ferroelectric BT ought to be minimised to ensure the proper formation of a core-shell structure in the BT grain [25]. Furthermore, it has been observed that as the ionic radius of the rare-earth oxides increases, a greater quantity of MgO is needed to establish a core-shell structure in the  $\text{MgO}\text{-Re}_2\text{O}_3\text{-BaTiO}_3$  system [26]. The sintering condition also significantly influences the development of the core-shell structure [22]. According to the XRD patterns presented in Figure 1b, 1 mol% of MgO was insufficient to create a core-shell structure for specimens sintered with  $\text{MgO}\text{-Y}_2\text{O}_3$  and/or  $\text{MgO}\text{-Dy}_2\text{O}_3$ . As a consequence, the  $\text{Y}^{3+}$  and  $\text{Dy}^{3+}$  ions might permeate the core grain, undermining the core-shell structure and revealing a tetragonal phase [25]. In contrast, the specimens sintered with MgO and co-sintered with  $\text{MgO}\text{-Yb}_2\text{O}_3$  exhibited a pseudo-cubic structure (ICCD No. 01-075-0212), evidenced by the fusion of the (002) and (200) planes in the XRD patterns. The diffusion of the  $\text{Yb}^{3+}$  ion (0.87 Å, CN = 6), which has a slightly smaller ionic radius than that of the  $\text{Y}^{3+}$  (0.9 Å, CN = 6) and  $\text{Dy}^{3+}$  ions (0.912 Å, CN = 6), was effectively inhibited by MgO in the specimens co-sintered with  $\text{MgO}\text{-Yb}_2\text{O}_3$ , resulting in the observed pseudo-cubic structure [27]. For the sintered specimens doped with MgO, MgO is substituted at the Ti site of BT due to the ionic radius of  $\text{Mg}^{2+}$  ions (0.72 Å) being similar to that of  $\text{Ti}^{4+}$  ions (0.605 Å) (Equation (3)), and the positively charged oxygen vacancy induces the deformation of BT from a tetragonal to a pseudo-cubic structure [12,27,28].



To obtain the lattice parameters of the sintered specimens, Rietveld refinement was performed on the XRD patterns, as shown in Figure 2. In the XRD data, the dotted line represents the observed intensity, while the solid line signifies the calculated intensity. The line at the base highlights the disparity between the observed and calculated values. Table 3 presents the R-factors and the lattice parameters derived from the Rietveld refinements for the sintered specimens. The goodness of fit (GoF) and the Bragg R-factor, serving as indicators of RIR, fell within the ranges of 1.9–2.6 and 1.79–2.87, respectively. These values suggest that the RIR data are highly reliable.

Figure 3a displays the unit-cell volumes of the BT specimens either doped with MgO or co-doped with  $\text{MgO}\text{-Re}_2\text{O}_3$  (with Re representing Y, Yb, or Dy) and sintered under an optimal sintering condition. The unit-cell volume of specimens co-doped with  $\text{MgO}\text{-Y}_2\text{O}_3$  and/or  $\text{MgO}\text{-Dy}_2\text{O}_3$  may be influenced by the substitution sites of  $\text{Y}^{3+}$  and  $\text{Dy}^{3+}$  ions within the BT lattice when intermediate rare-earth oxides, such as  $\text{Y}_2\text{O}_3$  and  $\text{Dy}_2\text{O}_3$ , are substituted into BT [16]. As previously mentioned, MgO replaces the Ti site of BT, leading to the  $\text{Y}^{3+}$  (1.234 Å, CN = 12) and  $\text{Dy}^{3+}$  ions (1.255 Å, CN = 12) primarily occupying the Ba site (1.61 Å, CN = 12) in specimens co-doped with  $\text{MgO}\text{-Y}_2\text{O}_3$  and/or  $\text{MgO}\text{-Dy}_2\text{O}_3$  [28]. Consequently, specimens co-doped with  $\text{MgO}\text{-Y}_2\text{O}_3$  and/or  $\text{MgO}\text{-Dy}_2\text{O}_3$  exhibited a smaller unit-cell volume compared to specimens solely doped with MgO. Conversely, the unit-cell volume of specimens co-doped with  $\text{MgO}\text{-Yb}_2\text{O}_3$  was akin to that of the MgO-doped specimens, owing to the  $\text{Yb}_2\text{O}_3$  substitution at the Ti site. Notably, prior research indicates that the  $\text{Yb}^{3+}$  ion (0.87 Å, CN = 6), due to its compact ionic radius, takes the place of the Ti site regardless of the Ba/Ti ratio [11,28].

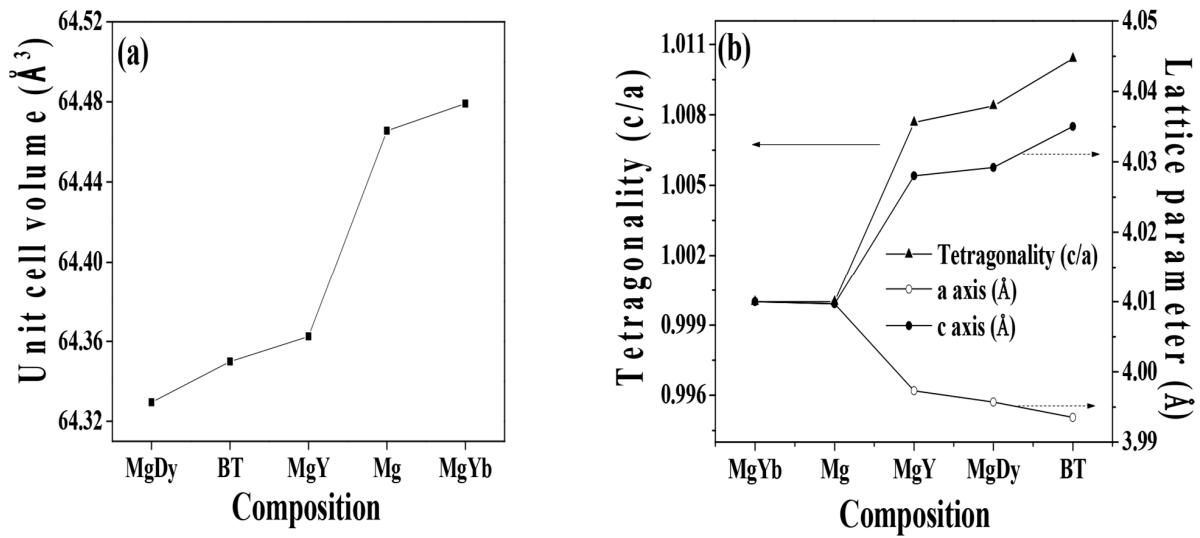


**Figure 2.** Rietveld refinement patterns of the sintered specimens: (a) doped with MgO, (b) co-doped with MgO-Yb<sub>2</sub>O<sub>3</sub>, (c) pure BT, (d) co-doped with MgO-Y<sub>2</sub>O<sub>3</sub>, (e) co-doped with MgO-Dy<sub>2</sub>O<sub>3</sub>.

**Table 3.** Lattice parameters of the sintered specimens and R-factors obtained from the Rietveld refinements.

Specimen	Lattice Parameter (Å)		Tetragonality (c/a)	Unit-Cell Volume (Å <sup>3</sup> )	R <sub>bragg</sub>	GoF
	a-Axis	c-Axis				
Pure BT	3.9935	4.0350	1.01039	64.3499	2.87	2.6
MgO-Dy <sub>2</sub> O <sub>3</sub>	3.9957	4.0292	1.00838	64.3294	2.30	2.3
MgO-Y <sub>2</sub> O <sub>3</sub>	3.9973	4.0280	1.00768	64.3625	2.35	2.4
MgO	4.0097	4.0097	1	64.4656	2.21	2.1
MgO-Yb <sub>2</sub> O <sub>3</sub>	4.0100	4.0100	1	64.4792	1.79	1.9

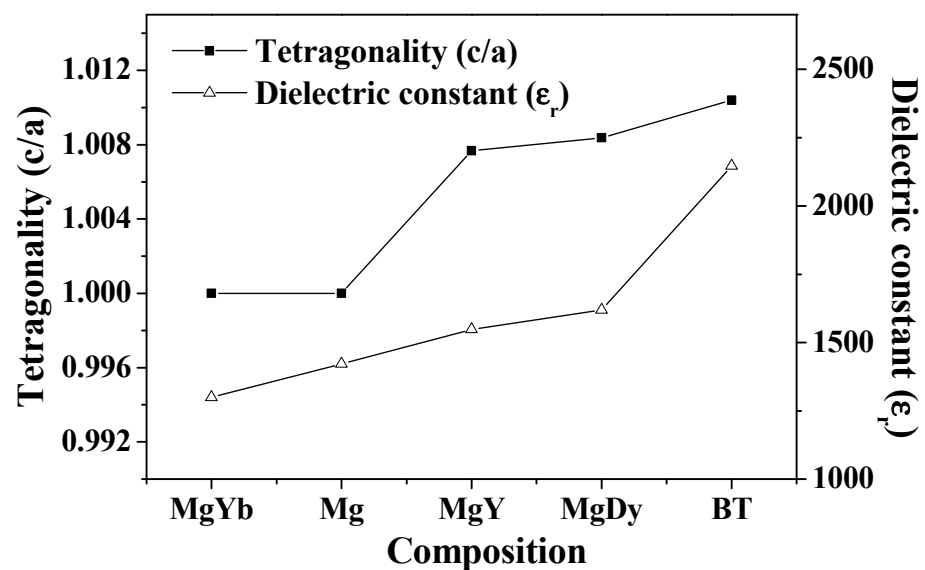
Figure 3b displays the lattice parameters and tetragonality of the BT specimens doped with MgO and/or co-doped with MgO-Re<sub>2</sub>O<sub>3</sub> (with Re representing Y, Yb, or Dy). The sintered specimens co-doped with MgO-Y<sub>2</sub>O<sub>3</sub> and MgO-Dy<sub>2</sub>O<sub>3</sub>, possessing a tetragonal structure, exhibited reduced tetragonality (c/a) in comparison to that of pure BT. This reduction can be attributed to the substitution of Dy<sup>3+</sup> and Y<sup>3+</sup> at the Ba site, leading to a marked decrease in the c-axis relative to the a-axis [29,30]. In contrast, the sintered specimens doped with MgO and co-doped with MgO-Yb<sub>2</sub>O<sub>3</sub> demonstrated a tetragonality (c/a = 1) lower than that of pure BT. This observation is linked to the presence of positively charged oxygen vacancies for the specimens doped with MgO and the emergence of a shell phase for the specimens co-doped with MgO-Yb<sub>2</sub>O<sub>3</sub>. For those sintered specimens with a pseudo-cubic structure, the a-axis and c-axis lattices within the perovskite framework align, negating any XRD pattern separation between the (002) and (200) planes.



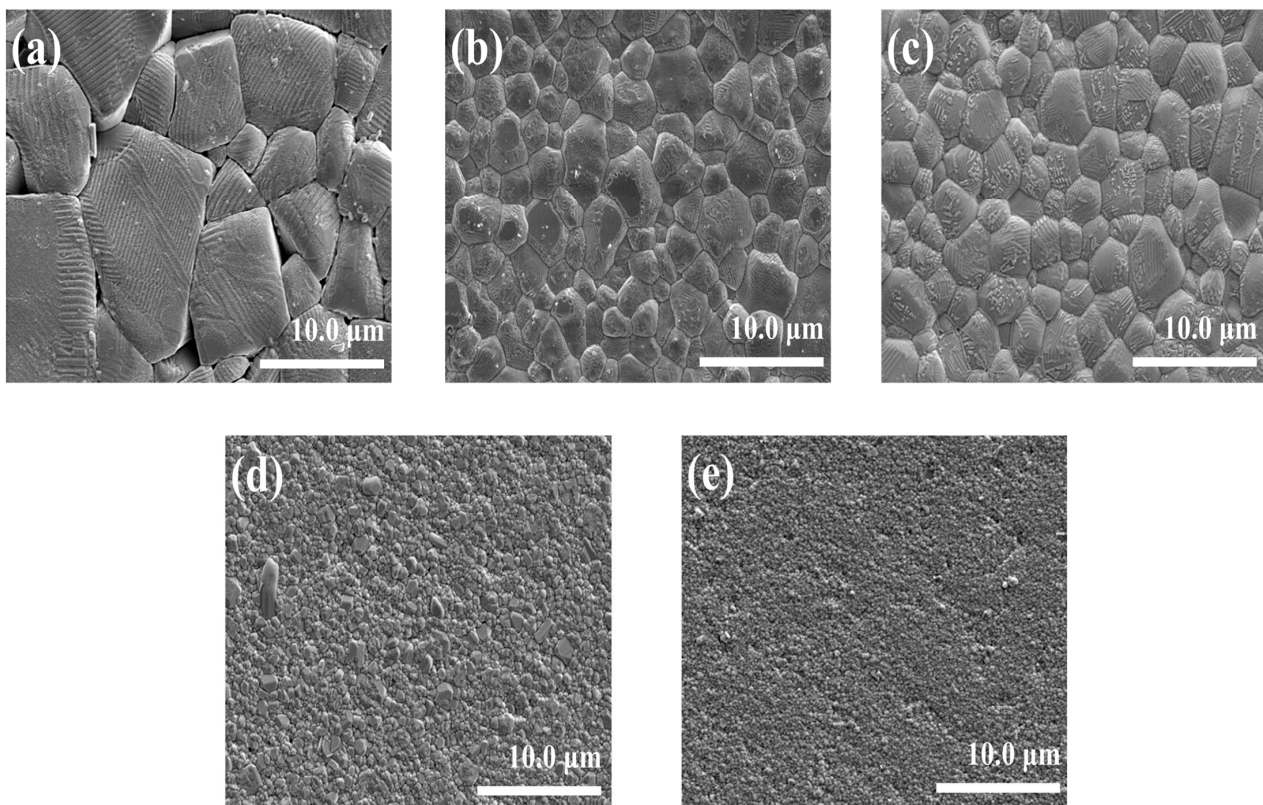
**Figure 3.** (a) Unit-cell volume and (b) lattice parameters of the BT specimens doped with MgO and/or co-doped with MgO-Re<sub>2</sub>O<sub>3</sub> (Re = Y, Yb, or Dy).

### 3.2. Dielectric and Electrical Properties

Figure 4 shows the dependence of the dielectric constant ( $\epsilon_r$ ) on the tetragonality ( $c/a$ ) of the BT specimens doped with MgO and/or co-doped with MgO-Re<sub>2</sub>O<sub>3</sub> (with Re representing Y, Yb, or Dy). With the substitution of MgO and rare-earth oxides, the sintered specimens showed a lower dielectric constant ( $\epsilon_r$ ) than that of pure BT. The dielectric constant ( $\epsilon_r$ ) is affected by the magnitude of spontaneous polarisation and the domain wall density and its mobility [31–34]. Because spontaneous polarisation is proportional to tetragonality ( $c/a$ ) [35], the dielectric constant ( $\epsilon_r$ ) of the sintered specimens doped with MgO and/or rare-earth oxides decreased with the decrease of tetragonality, which restricts the moving space of the Ti<sup>4+</sup> ion in the [TiO<sub>6</sub>] octahedron. Although the tetragonality of the sintered specimens co-doped with MgO-Yb<sub>2</sub>O<sub>3</sub> and doped with MgO are the same, the  $\epsilon_r$  of the sintered specimens doped with MgO was slightly larger than that of the sintered specimens co-doped with MgO-Yb<sub>2</sub>O<sub>3</sub> due to the larger grain size at the submicron level, as confirmed in Figure 5.



**Figure 4.** Dependence of the dielectric constant ( $\epsilon_r$ ) on the tetragonality ( $c/a$ ) of the BT specimens doped with MgO and/or co-doped with MgO-Re<sub>2</sub>O<sub>3</sub> (Re = Y, Yb, or Dy).



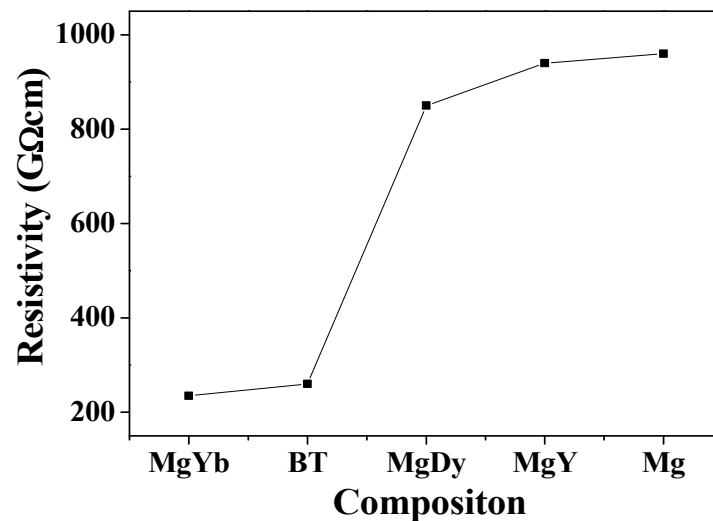
**Figure 5.** Scanning electron micrographs of the sintered specimens: (a) pure BT, (b) co-doped with MgO-Y<sub>2</sub>O<sub>3</sub>, (c) co-doped with MgO-Dy<sub>2</sub>O<sub>3</sub>, (d) doped with MgO, and (e) co-doped with MgO-Yb<sub>2</sub>O<sub>3</sub> (scale bar: 10 μm).

Figure 5 presents SEM micrographs detailing the surface structures of the BT specimens, either doped with MgO or co-doped with MgO-Re<sub>2</sub>O<sub>3</sub> (with Re representing Y, Yb, or Dy). All sintered specimens exhibited dense microstructures, aligning with relative densities exceeding 94%, as documented in Table 2. The pure BT manifested the most prominent grain size, accompanied by abnormal grain growth. Upon introducing MgO and rare-earth oxides, the grain size of the sintered specimens was observed to be more diminutive compared to that of pure BT. This reduction is attributed to the grain growth inhibition properties of MgO and the rare-earth oxides during the sintering process [11–13,17]. Specimens co-doped with MgO-Y<sub>2</sub>O<sub>3</sub> and MgO-Dy<sub>2</sub>O<sub>3</sub> displayed comparable grain sizes. Conversely, those doped with MgO and co-doped with MgO-Yb<sub>2</sub>O<sub>3</sub> demonstrated considerably finer grain sizes than their counterparts co-doped with MgO-Y<sub>2</sub>O<sub>3</sub> and MgO-Dy<sub>2</sub>O<sub>3</sub>.

Figure 6 illustrates the electrical resistivity ( $\rho$ ) of the BT specimens either doped with MgO or co-doped with MgO-Re<sub>2</sub>O<sub>3</sub> (with Re representing Y, Yb, or Dy). The sintered specimens doped with MgO, as well as those co-doped with MgO-Y<sub>2</sub>O<sub>3</sub> and MgO-Dy<sub>2</sub>O<sub>3</sub>, exhibited an elevated electrical resistivity value of 850 G $\Omega$  (500 V, 60 s) or higher, approximately thrice that of pure BT. This enhancement is attributed to the grain size reduction mediated by MgO, Y<sub>2</sub>O<sub>3</sub>, and Dy<sub>2</sub>O<sub>3</sub>, all of which act as grain growth inhibitors, as previously discussed [36,37]. In contrast, specimens co-doped with MgO-Yb<sub>2</sub>O<sub>3</sub> displayed electrical resistivity analogous to pure BT despite the grain size reduction. This behaviour can likely be ascribed to the pyrochlore phase of Yb<sub>2</sub>Ti<sub>2</sub>O<sub>7</sub>, a noted high ionic conductor [38]. Prior research has also indicated that the pyrochlore phase expedites the migration of oxygen vacancies, a primary factor in insulation degradation [39].

To assess the temperature stability of the sintered specimens, the TCC was gauged from  $-50$  °C to  $150$  °C at 1 KHz. Figure 7a depicts the temperature-dependent dielectric constant ( $\epsilon_r$ ) for BT specimens either doped with MgO or co-doped with MgO-Re<sub>2</sub>O<sub>3</sub> (with Re representing Y, Yb, or Dy). Specimens co-doped with MgO-Y<sub>2</sub>O<sub>3</sub> and MgO-Dy<sub>2</sub>O<sub>3</sub>

exhibited a pronounced dielectric peak near 100 °C, with the Curie temperature ( $T_c$ ) for each specimen marginally dropping to 99 °C and 103 °C, as seen in Figure 7a. For specimens doped with MgO that display a cubic structure, there was a broadening of the dielectric peak accompanied by a shift in the Curie temperature. The TCCs for the BT specimens doped with MgO and/or co-doped with MgO- $\text{Re}_2\text{O}_3$  (with Re representing Y, Yb, or Dy) are presented in Figure 7b. As previously mentioned, the BT specimens with MgO doping exhibited a flattened TCC curve alongside a reduction in Curie temperature. This observed behaviour met the X8R specification ( $-55\sim 150$  °C,  $\Delta C/C$  approximately  $\pm 15\%$ ) of the EIA classification, stemming from the introduction of oxygen vacancies by the substitution of  $\text{Mg}^{2+}$  ions at the Ti site. This trend aligns with previous studies on MgO-doped BT [12]. For enhanced temperature stability in rare-earth oxide-doped  $\text{BaTiO}_3$ , a diminished transition peak is essential. The predominant factor influencing the spread of the Curie temperature appears to be the internal microstructural stress caused by the transition from tetragonal to cubic structures in BT [11,40]. It appears that the phase transition was not effectively realised in specimens co-doped with MgO- $\text{Y}_2\text{O}_3$  and MgO- $\text{Dy}_2\text{O}_3$ , failing to meet the X8R specification. However, the transition was prominent in specimens co-doped with  $\text{MgOYb}_2\text{O}_3$ , which adhered to the X7R specification.



**Figure 6.** Electrical resistivities of BT specimens doped with MgO and/or co-doped with MgO- $\text{Re}_2\text{O}_3$  (Re = Y, Yb, or Dy).

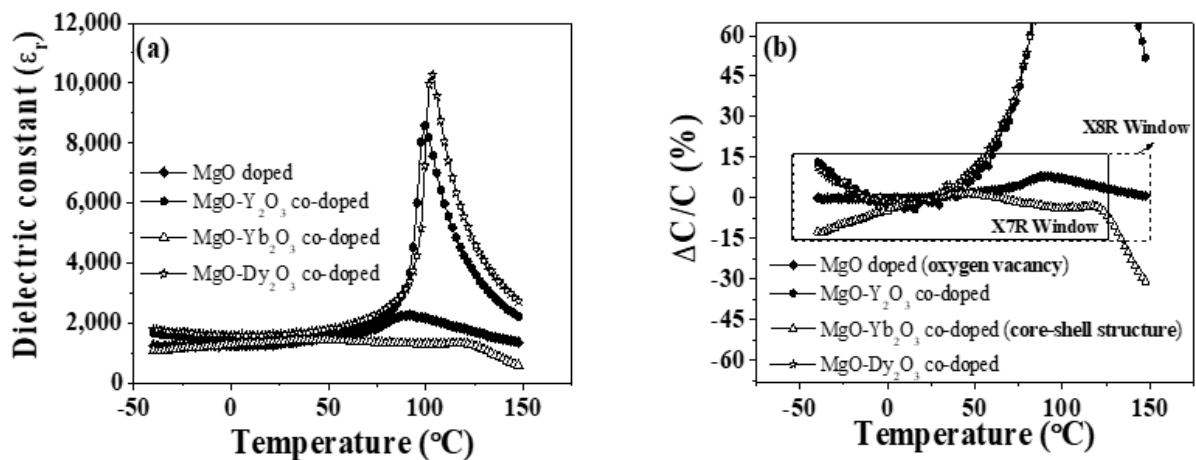


**Figure 7.** (a) Temperature dependence of the dielectric constant ( $\epsilon_r$ ) and (b) temperature coefficient of capacitance (TCC) of BT specimens doped with MgO and/or co-doped with MgO- $\text{Re}_2\text{O}_3$  (Re = Y, Yb, or Dy).

#### 4. Conclusions

The effects of MgO and rare-earth oxides ( $Y_2O_3$ ,  $Yb_2O_3$ , and  $Dy_2O_3$ ) on the structural and electrical properties of  $BaTiO_3$  have been investigated. For specimens sintered at  $1350\text{ }^\circ\text{C}$  for durations ranging from 1 to 5 h in air, a single phase of  $BaTiO_3$  with a tetragonal structure was identified in pure BT and BT specimens co-doped with MgO- $Y_2O_3$  and/or MgO- $Dy_2O_3$ . However, for specimens doped with MgO or MgO- $Yb_2O_3$ ,  $BaTiO_3$  with a pseudo-cubic structure was detected. A secondary phase of  $Yb_2Ti_2O_7$  was identified in BT specimens co-doped with MgO and  $Yb_2O_3$ , attributed to the limited solubility of the  $Yb^{3+}$  ions in the BT lattice. These results indicate a smaller unit-cell volume in BT specimens co-doped with MgO- $Y_2O_3$  and MgO- $Dy_2O_3$  compared to that of BT specimens doped solely with MgO, suggesting that the  $Y^{3+}$  and  $Dy^{3+}$  ions are substituted at the Ba site of BT. With the introduction of MgO and rare-earth oxides, the dielectric constant ( $\epsilon_r$ ) of the sintered specimens decreased, which was associated with a reduction in tetragonality ( $c/a$ ) that limited the mobility of the  $Ti^{4+}$  ion within the  $TiO_6$  octahedron. The electrical resistivity of the sintered specimens increased with reductions of the grain size in BT specimens doped with MgO and/or co-doped with MgO- $Re_2O_3$  ( $Re = Y$  or  $Dy$ ). BT specimens co-doped with MgO- $Yb_2O_3$  and/or MgO met the EIA X7R ( $-55$  to  $125\text{ }^\circ\text{C}$ ,  $\Delta C/C$  of  $\pm 15\%$  or less) and X8R specifications ( $-55$  to  $150\text{ }^\circ\text{C}$ ,  $\Delta C/C$  of  $\pm 15\%$  or less), respectively.

**Author Contributions:** E.S.K. and J.H.P. designed the experiments. J.H.P. performed the experiments and analysed the specimens. E.S.K. analysed and explained the dependence of the electrical properties on the microstructure behaviours of the specimens. E.S.K. and J.H.P. discussed the data and prepared the manuscript. All authors have read and agreed to the published version of the manuscript.

**Funding:** This work was supported by the Technology Innovation (20010938, Development of 630 V high capacity MLCC array module for power train), funded by the Ministry of Trade, Industry, and Energy (MOTIE, Sejong City, Republic of Korea).

**Data Availability Statement:** Data are contained within the article.

**Conflicts of Interest:** The authors declare no conflict of interest.

#### References

1. Pu, Y.; Chen, W.; Chen, S.; Langhammer, H.T. Microstructure and dielectric properties of dysprosium-doped barium titanate ceramics. *Ceramica* **2005**, *51*, 214–218. [[CrossRef](#)]
2. Hao, H.; Liu, M.; Liu, H.; Zhang, S.; Shu, X.; Wang, T.; Yao, Z.; Cao, M. Design, Fabrication and dielectric properties on core-double shell  $BaTiO_3$ -based ceramics for MLCC application. *RSC Adv.* **2015**, *5*, 8868–8876. [[CrossRef](#)]
3. Zhang, Y.; Wang, X.; Kim, J.Y.; Tian, Z.; Fang, J.; Hur, K.H.; Li, L. High performance of  $BaTiO_3$ -Based BME MLCC Nanopowder Prepared by Aqueous Chemical Coating method. *J. Am. Ceram. Soc.* **2012**, *95*, 1628–1633. [[CrossRef](#)]
4. Hernandez, V.I.; García-Guti, D.I.; Aguilar-Garib, J.A.; Nava-Quintero, R.J. Characterization of precipitates formed in X7R 0603 BME-MLCC during sintering. *Ceram. Int.* **2021**, *47*, 310–319. [[CrossRef](#)]
5. MYoon, M.S.; Ur, S.C. Effects of A-site Ca and B-site Zr substitution on dielectric properties and microstructure in tin-doped  $BaTiO_3$ - $CaTiO_3$  composites. *Ceram. Int.* **2008**, *34*, 1941–1948.
6. Zhu, X.; Zhu, J.; Zhou, S.; Liu, Z.; Ming, N.; Hesse, D.  $BaTiO_3$  nanocrystals: Hydrothermal synthesis and structural characterization. *J. Cryst. Growth* **2005**, *283*, 553–562. [[CrossRef](#)]
7. Beck, H.P.; Eiser, W.; Haberkorn, R. Pitfalls in the synthesis of nanoscaled perovskite type compounds. Part I: Influence of different sol-gel preparation methods and characterization of nanoscaled  $BaTiO_3$ . *J. Eur. Ceram. Soc.* **2001**, *21*, 687–693. [[CrossRef](#)]
8. Shimooka, H.; Kuwabara, M. Crystallinity and Stoichiometry of Nano-Structured Sol-Gel Derived  $BaTiO_3$  Monolithic Gels. *J. Am. Ceram. Soc.* **1996**, *79*, 2983–2985. [[CrossRef](#)]
9. Wei, X.; Xu, G.; Ren, Z.; Shen, G.; Han, G. Room-Temperature Synthesis of  $BaTiO_3$  Nanoparticles in Large Batches. *J. Am. Ceram. Soc.* **2008**, *91*, 3774–3780. [[CrossRef](#)]
10. Kozerozhets, I.; Semenov, E.; Kozlova, L.; Ioni, Y.; Avdeeva, V.; Ivakin, Y. Mechanism to form nanosized oxides when burning aqueous carbohydrate salt solutions. *Mater. Chem. Phys.* **2023**, *309*, 128387. [[CrossRef](#)]
11. Song, Y.H.; Han, Y.H. Effects of Rare-Earth Oxides on Temperature Stability of Acceptor-Doped  $BaTiO_3$ . *Jpn. J. Appl. Phys.* **2005**, *44*, 6143. [[CrossRef](#)]

12. Jeong, J.; Han, Y.H. Effects of MgO-Doping on Electrical Properties and Microstructure of BaTiO<sub>3</sub>. *Jpn. J. Appl. Phys.* **2004**, *43*, 5373. [[CrossRef](#)]
13. Kim, C.H.; Park, K.J.; Yoon, Y.J.; Hong, M.H.; Hong, J.O.; Hur, K.H. Role of Yttrium and magnesium in the formation of core-shell structure of BaTiO<sub>3</sub> grains in MLCC. *J. Eur. Ceram. Soc.* **2008**, *28*, 1213–1219. [[CrossRef](#)]
14. Sakabe, Y.; Hamaji, Y.; Sano, H.; Wada, N. Effects of Rare-Earth Oxides on the Reliability of X7R Dielectrics. *Jpn. J. Appl. Phys.* **2002**, *41*, 5668. [[CrossRef](#)]
15. Saito, H.; Chazono, H.; Kishi, H.; Yamaoka, N. X7R Multilayer Ceramic Capacitors with Nickel Electrodes. *Jpn. J. Appl. Phys.* **1991**, *30*, 2307. [[CrossRef](#)]
16. Park, K.J.; Kim, C.H.; Yoon, Y.J.; Song, S.M.; Kim, Y.T.; Hur, K.H. Doping behaviors of dysprosium, yttrium and holmium in BaTiO<sub>3</sub> ceramics. *J. Eur. Ceram. Soc.* **2009**, *29*, 1735–1741. [[CrossRef](#)]
17. Li, Y.X.; Yao, X.; Wang, X.S.; Hao, Y.B. Studies of dielectric properties of rare earth (Dy, Tb, Eu) doped barium titanate sintered in pure nitrogen. *Ceram. Int.* **2012**, *38*, S29–S32. [[CrossRef](#)]
18. Wang, M.; Xue, K.; Zhang, K.; Li, L. Dielectric properties of BaTiO<sub>3</sub>-based ceramics are tuned by defect dipoles and oxygen vacancies under a reducing atmosphere. *Ceram. Int.* **2022**, *48*, 22212–22220. [[CrossRef](#)]
19. Kishi, H.; Okino, Y.; Honda, M.; Iguchi, Y.; Imaeda, M.; Takahashi, Y.; Ohsato, H.; Okuda, T. The effect of MgO and rare-earth oxide on formation behavior of core-shell structure in BaTiO<sub>3</sub>. *Jpn. J. Appl. Phys.* **1997**, *36*, 5954. [[CrossRef](#)]
20. Yang, W.C.; Hu, C.T.; Lin, I.N. Effect of Y<sub>2</sub>O<sub>3</sub>/MgO Co-doping on the electrical properties of base-metal-electroded BaTiO<sub>3</sub> materials. *J. Eur. Ceram. Soc.* **2004**, *24*, 1479–1483. [[CrossRef](#)]
21. Wang, S.; Zhang, S.; Zhou, X.; Li, B.; Chen, Z. Effect of sintering atmospheres on the microstructure and dielectric properties of Yb/Mg co-doped BaTiO<sub>3</sub> ceramics. *Mater. Lett.* **2005**, *59*, 2457–2460. [[CrossRef](#)]
22. Gong, H.; Wang, X.; Zhang, S.; Yang, X.; Li, L. Influence of sintering temperature on core-shell structure evolution and reliability in Dy modified BaTiO<sub>3</sub> dielectric ceramics. *Phys. Status Solidi* **2014**, *211*, 1213–1218. [[CrossRef](#)]
23. Hahn, D.W.; Han, Y.H. Electrical properties of Yb-Doped BaTiO<sub>3</sub>. *Jpn. J. Appl. Phys.* **2009**, *48*, 111406. [[CrossRef](#)]
24. Nfissi, A.; Ababou, Y.; Belhajji, M.; Sayouri, S.; Hajji, L.; Bennani, M.N. Investigation of Ba and Ti site occupation effects on structural, optical and dielectric properties of sol gel processed Y-doped BaTiO<sub>3</sub> ceramics. *Opt. Mater.* **2021**, *122*, 111708. [[CrossRef](#)]
25. Liu, R.; Chen, Z.; Lu, Z.; Wang, X. Effects of sintering temperature and Bi<sub>2</sub>O<sub>3</sub>, Y<sub>2</sub>O<sub>3</sub> and MgO co-doping on the dielectric properties of X8R BaTiO<sub>3</sub>-based ceramics. *Ceram. Int.* **2022**, *48*, 2377–2384. [[CrossRef](#)]
26. Kishi, H.; Kohzu, N.; Sugino, J.; Ohsato, H.; Iguchi, Y.; Okuda, T. The effect of Rare-earth (La, Sm, Dy, Ho and Er) and Mg on the microstructure in BaTiO<sub>3</sub>. *J. Eur. Ceram. Soc.* **1999**, *19*, 1043–1046. [[CrossRef](#)]
27. Lin, Y.T.; Ou, S.F.; Lin, M.H.; Song, Y.R. Effect of MgO addition on the microstructure and dielectric properties of BaTiO<sub>3</sub> ceramics. *Ceram. Int.* **2018**, *44*, 3531–3535.
28. Shannon, R.D. Revised effective ionic radii and systematic studies of interatomic distances in halides and chalcogenides. *Acta Cryst.* **1976**, *32*, 751–766. [[CrossRef](#)]
29. Badapanda, T.; Senthil, V.; Panigrahi, S.; Anwar, S. Diffuse of phase transition behavior of dysprosium doped barium titanate ceramic. *J. Electroceram.* **2013**, *31*, 55–60. [[CrossRef](#)]
30. Tihtih, M.; Ibrahim, J.E.F.M.; Basyooni, M.A.; En-nadir, R.; Belaid, W.; Hussainova, I.; Kocserha, I. Development of yttrium-doped BaTiO<sub>3</sub> for next-generation multilayer ceramic capacitors. *ACS Omega* **2023**, *8*, 8448–8460. [[CrossRef](#)] [[PubMed](#)]
31. Arlt, G.; Hennings, D.; de With, G. Dielectric properties of fine-grained barium titanate ceramics. *J. Appl. Phys.* **1985**, *58*, 1619–1625. [[CrossRef](#)]
32. Yoon, S.H.; Kim, S.J.; Kim, D.Y. Influence of excess Ba concentration on the dielectric nonlinearity in Mn and V-doped BaTiO<sub>3</sub> multilayer ceramic capacitors. *J. Appl. Phys.* **2013**, *114*, 224103. [[CrossRef](#)]
33. Yoon, S.H.; Kim, M.Y.; Nam, C.H.; Seo, J.W.; Wi, S.K.; Hur, K.H. Correlation between tetragonality (c/a) and direct current (dc) bias characteristics of BaTiO<sub>3</sub>-based multilayer ceramic capacitors. *Appl. Phys. Lett.* **2015**, *107*, 072906. [[CrossRef](#)]
34. Tutuncu, G.; Li, B.; Bowman, K.; Jones, J.L. Domain wall motion and electromechanical strain in lead free piezoelectrics: Insight from the model system (1-x)Ba(Zr<sub>0.2</sub>Ti<sub>0.8</sub>)O<sub>3</sub>-x(Ba<sub>0.7</sub>Ca<sub>0.3</sub>)TiO<sub>3</sub> using in situ high-energy X-ray diffraction during application of electric fields. *J. Appl. Phys.* **2014**, *115*, 144104. [[CrossRef](#)]
35. Qi, T.; Grinberg, I.; Rappe, A.M. Correlations between tetragonality, A.M.R.; polarization, and ionic displacement in PbTiO<sub>3</sub>-derived ferroelectric perovskite solid solutions. *Phys. Rev. B* **2010**, *82*, 134113. [[CrossRef](#)]
36. Gong, H.; Wang, X.; Zhang, S.; Wen, H.; Li, L. Grain size effect on electrical and reliability characteristics of modified fine-grained BaTiO<sub>3</sub> ceramics for MLCCS. *J. Eur. Ceram. Soc.* **2014**, *34*, 1733–1739. [[CrossRef](#)]
37. Yoon, S.H.; Randall, C.A.; Hur, K.H. Influence of Grain Size on Impedance Spectra and Resistance Degradation Behavior in Acceptor (Mg)-Doped BaTiO<sub>3</sub> Ceramics. *J. Am. Ceram. Soc.* **2009**, *92*, 2944–2952. [[CrossRef](#)]
38. Shlyakhtina, A.; Fedtke, P.; Busch, A.; Kolbanev, I.; Barfels, T.; Wienecke, M.; Sokolov, A.; Ulianov, V.; Trounov, V.; Shcherbakova, L. Effect of Ca-doping on the electrical conductivity of oxide ion conductor Yb<sub>2</sub>Ti<sub>2</sub>O<sub>7</sub>. *Solid State Ion.* **2008**, *179*, 1004–1008. [[CrossRef](#)]

39. Yoon, S.H.; Park, Y.S.; Hong, J.O.; Sinn, D.S. Effect of pyrochlore ( $Y_2Ti_2O_7$ ) phase on the resistance degradation on yttrium-doped  $BaTiO_3$  ceramic capacitors. *J. Mater. Res.* **2007**, *22*, 2539–2543. [[CrossRef](#)]
40. Hennings, D.; Schnell, A.; Simon, G. Diffuse Ferroelectric Phase Transitions in  $Ba(Ti_{1-y}Zr_y)O_3$  ceramics. *J. Am. Ceram. Soc.* **1982**, *65*, 539–544. [[CrossRef](#)]

**Disclaimer/Publisher’s Note:** The statements, opinions and data contained in all publications are solely those of the individual author(s) and contributor(s) and not of MDPI and/or the editor(s). MDPI and/or the editor(s) disclaim responsibility for any injury to people or property resulting from any ideas, methods, instructions or products referred to in the content.